Attenuated Self-Interference Synchrophasor Estimation: the SOGI Interpolated DFT

César García-Veloso
Department of Electrical Engineering
University of Seville
Seville, Spain
cgveloso@us.es

Mario Paolone
Distributed Electrical Systems Laboratory
École Polytechnique Fédérale de Lausanne
Lausanne, Switzerland
mario.paolone@epfl.ch

José María Maza-Ortega
Department of Electrical Engineering
University of Seville
Seville, Spain
jmmaza@us.es

***Abstract*—In this paper, a synchrophasor estimation (SE) algorithm is presented to simultaneously comply with the requirements for the P and M phasor measurement unit (PMU) performance classes. The method employs a second-order generalized integrator (SOGI) quadrature signal generator (QSG) filter to attenuate the self-interference of the fundamental tone. Inspired by other static state-of-the-art SE methods, the algorithm combines a three-point IpDFT with a three-cycle Hanning window delivering a reduction in the total computational cost. Its performance with respect to all the operating conditions defined by the IEC/IEEE Std. 60255-118 is assessed and compared with another state-of-the-art technique. Furthermore, a computational complexity analysis is performed to assess the potential viability of the proposed SE algorithm for its implementation in embedded devices.**

***Index Terms*—IEC/IEEE Std 60255-118-1-2018, second-order generalized integrator, discrete Fourier transform, interpolated DFT, phasor measurement unit, synchrophasor estimation.**

I. Introduction

Although most commercial PMUs rely on DFT-based synchrophasor estimation (SE) algorithms [1], which are capable of delivering accurate estimates by simply processing a few DFT bins [2], two main limitations bound their performance: aliasing and spectral leakage. The adoption of higher sampling rates and/or anti-aliasing filters may tackle aliasing, while short- and long-range spectral leakage[1] are addressed by modern interpolated DFT techniques (IpDFT), respectively, by interpolating the DFT bins [3] and windowing [4]. Self-interference, namely, the mutual interaction between the positive and negative spectral images, represents the main source of error in DFT-based SE processes [5]. In a real-valued power system signal, whose main tone nominal frequency is close to DC, this phenomenon is further enhanced due to the general adoption of short analysis windows of just a few nominal cycles [5]–[7] used to comply with both the latency requirements of [8] and the assumption of a discrete signal spectrum.

Different techniques have been proposed to attenuate negative image infiltration. Some of the most relevant in SE are the multi-point weighted IpDFT [9], new cosine windows called Maximum Image interference Rejection with Rapid Sidelobe Decay rate (MIR-RSD) windows with high rejection of self-interference [10], the iterative approximation and compensation of the negative image based on DFT symmetry [6] and the approximation of the analytic signal by a Hilbert filter to remove the negative spectrum [5]. Another suitable way to cancel the negative image of a specific tone is to define a complex signal $(\bar{y})$ with in-quadrature real (y_α) and imaginary (y_β) components at the frequency of the tone of interest and of the same magnitude (see Section II-B). This is done in [11] where a SE technique is presented which relies on a delayed in-quadrature complex signal generation technique to mitigate the self-interference of the fundamental tone. This paper proposes a SE algorithm that employs a second-order generalized integrator (SOGI) quadrature signal generator (QSG) filter to obtain such a signal $(\bar{y})$ and attenuate the effects of self-interference. The method, named SOGI-IpDFT, is built on the same three-point IpDFT combined with a Hanning window and OOBI detection mechanism used by the i-IpDFT [7], [12]. Moreover, it also uses a similar iterative formulation to remove the effects of OOBIs and ensure compliance with all requirements for both PMU classes. Compared to the i-IpDFT, a reduced computational cost is achieved in return for a higher signal buffer size. The remainder of the paper is organized as follows. Section II provides the fundamentals of SE IpDFT-based methods and of SOGI-QSG. Section III presents the structure, formulation, parameterization, and computational cost of the SOGI-IpDFT algorithm. Section IV evaluates its performance based on the P- and M-class PMUs defined in [8] and compares it with the i-IpDFT algorithm proposed in [7], [12]. Given their comparative performance, section V proposes a merged structure, named eSOGI-IpDFT, based on the combination of both algorithms. Finally, Section VI provides some closing remarks.

II. Fundamentals of IpDFT SE and SOGI-QSG

This section presents the fundamentals of the SOGI-IpDFT algorithm, namely: (i) the three-point (3p) IpDFT based on

The project that gave rise to these results received the support of a fellowship from "la Caixa" Foundation (ID 100010434). The fellowship code is LCF/BQ/DR20/11790026.

[1]Short-range leakage is the error associated with the displacement of the maximum bin while long-range leakage is caused by the mutual interference between all tones that form the spectrum of the signal.

the Hanning window; (ii) the attenuation of self-interference through in-quadrature signals; and (iii) the SOGI-QSG filter.

A. Three-point IpDFT based on the Hanning window

The same IpDFT formulation used in [5], [7] is used for the SOGI-IpDFT. It considers a three-point DFT interpolation scheme that reduces the effects of long-range leakage [9] and a Hanning window function as it offers a good compromise between sidelobe decay and mainlobe width [13].

$$x(n) = A_0 \cos(2\pi f_0 n T_s + \varphi_0), \quad n \in [0, N-1] \tag{1}$$

Given a set of N samples $x(n)$ (1) taken from a continuous single-tone steady state signal $x(t)$ with sampling period T_s, the 3p Hanning IpDFT provides an analytical formulation to determine its defining parameters, i.e. its fundamental frequency f_0 (3a), amplitude A_0 (3b) and initial phase φ_0 (3c), based on a fractional correction term δ_H (2):

$$\delta_H = 2\varepsilon \frac{|X_H(k_m+\varepsilon)| - |X_H(k_m-\varepsilon)|}{|X_H(k_m-\varepsilon)| + 2|X_H(k_m)| + |X_H(k_m+\varepsilon)|} \tag{2}$$

where $\varepsilon = \pm 1$ if $|X_H(k_m+1)| \gtrless |X_H(k_m-1)|$, $X_H(k)$ is the Hanning windowed DFT spectrum of $x(n)$ and k_m the index of the highest bin. The term $\delta_H \in [-0.5, 0.5)$ represents the displacement of the fundamental with respect to the maximum bin k_m in the general case of incoherent sampling[2].

$$f_{0_H} = (k_m + \delta_H)\Delta_f \tag{3a}$$

$$A_{0_H} = 2|X_H(k_m)| \left| \frac{\pi\delta_H}{\sin(\pi\delta_H)} \right| |\delta_H^2 - 1| \tag{3b}$$

$$\varphi_{0_H} = \angle X_H(k_m) - \pi\delta_H \tag{3c}$$

where $\Delta f = 1/T$ is the DFT frequency resolution. The expressions (2)-(3) assume that no aliasing is present and that the DFT bins $X_H(k)$ are only the result of the positive image of the tone of interest. Finally, once a set of estimates of the signal parameters $(\hat{f}, \hat{A}, \hat{\varphi})$ is available, the spectral contributions of positive and negative images can be estimated by:

$$\hat{X}_{H\pm}(k) = \hat{A} e^{\pm j\hat{\varphi}} W_H(k \mp \hat{f}/\Delta_f) \tag{4}$$

where $W_H(k)$ is the DFT of the Hanning window.

B. Attenuated Self-Interference through in-quadrature signals

Consider a complex discrete single-tone steady-state signal $\bar{y}(n)$, with in-quadrature components $y_\alpha(n)$ and $y_\beta(n)$:

$$\bar{y}(n) = \underbrace{A_0 \cos(\omega_0 n T_s)}_{y_\alpha(n)} + j\, \underbrace{\xi A_0 \sin(\omega_0 n T_s)}_{y_\beta(n)}, \; n \in \mathbb{N} \tag{5}$$

where $\omega_0 = 2\pi f_0$ is the angular frequency[3] of the signal's fundamental tone and ξ is the ratio between the magnitudes of $y_\beta(n)$ and $y_\alpha(n)$. If (5) is expressed in terms of complex exponentials and the positive and negative frequency components are grouped, the following expression is obtained:

$$\bar{y}(n) = \frac{1}{2} A_0 (\underbrace{e^{j\theta_0(n)}(1+\xi)}_{\text{Positive Frequency}} + \underbrace{e^{-j\theta_0(n)}(1-\xi)}_{\text{Negative Frequency}}), \; n \in \mathbb{N} \tag{6}$$

where $\theta_0(n) = \omega_0 n T_s$. In the case of equimagnitude components ($\xi = 1$) the negative frequency component is cancelled and the positive one doubled. Nonetheless, even if the in-quadrature components $y_\alpha(n)$ and $y_\beta(n)$ have similar magnitudes ($\xi \simeq 1$), a major attenuation of the negative frequency component, and thus of self-interference, is achieved.

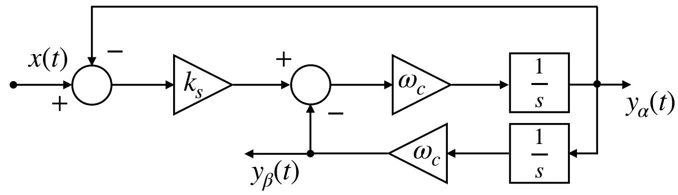

Fig. 1. Block diagram of the SOGI-QSG for a fixed centre frequency ω_c.

C. SOGI-QSG

The SOGI-QSG is a popular QSG method, widely used in single-phase PLLs, which not only generates in-quadrature signals, but also attenuates the harmonic components of the input signal [14]. It constitutes a second-order adaptive filter [15] whose block diagram for a fixed centre frequency ω_c is shown in Fig. 1[4]. Given an input signal $x(t)$, it generates two in-quadrature output signals $y_\alpha(t)$ and $y_\beta(t)$, whose transfer functions are given by:

$$G_\alpha(s) = \frac{y_\alpha(s)}{x(s)} = \frac{k_s \omega_c s}{s^2 + k_s \omega_c s + \omega_c^2} \tag{7a}$$

$$G_\beta(s) = \frac{y_\beta(s)}{x(s)} = \frac{k_s \omega_c^2}{s^2 + k_s \omega_c s + \omega_c^2} \tag{7b}$$

where s denotes the complex frequency, ω_c is the filter centre frequency, and k_s is the SOGI-QSG gain. As indicated in [15] k_s can be calculated to obtain a dynamic response with a desired settling time t_s according to:

$$k_s = \frac{9.2}{t_s \omega_c} \tag{8}$$

For ω_c equal to the nominal angular grid frequency ($2\pi f_n$) and t_s equal to one nominal electric cycle (20 ms for $f_n = 50$ Hz), Fig. 2 shows the frequency response of the SOGI-QSG filter for a normalized frequency $f[\mathrm{pu}] = f/f_n$. It can be seen that, across the spectrum, signals $y_\alpha(t)$ and $y_\beta(t)$ are guaranteed to be in-quadrature but only at f_n their magnitudes are the same. The filter response for any generic tone 'γ' of frequency f_γ can be calculated by evaluating (7) at $s = j2\pi f_\gamma$. The resulting complex values $\sigma_{\alpha_\gamma} = G_\alpha(j2\pi f_\gamma)$ and $\sigma_{\beta_\gamma} = G_\beta(j2\pi f_\gamma)$, defined as the complex α-β gains, indicate respectively the gain and phase shift introduced by the filter to the α-β

[2]As known, incoherent sampling refers to the adoption of a window length (T) which does not contain an integer number of periods of the signal fundamental tone ($1/f_0$), i.e., $\delta_H \neq 0$.

[3]Although for simplicity the initial angle has been set to 0, the same result holds if considered.

[4]The general implementation of the SOGI-QSG considers the centre frequency of the filter ω_c to be an adaptive parameter.

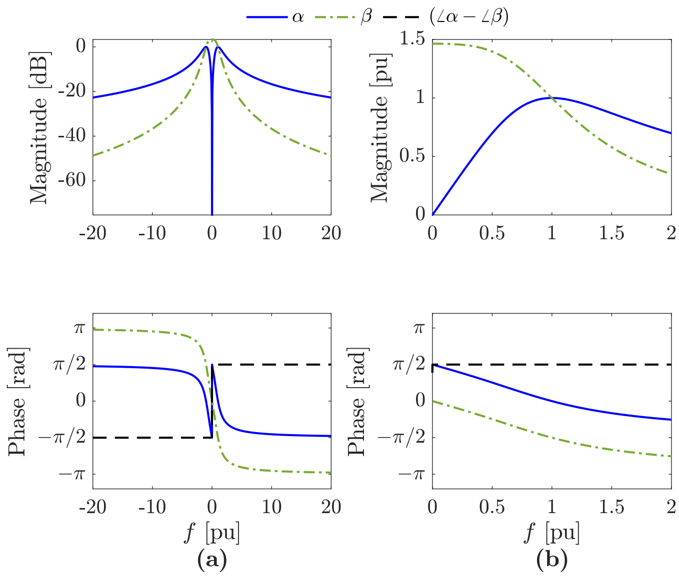

Fig. 2. Frequency response of SOGI-QSG for normalized frequency $f\,[\mathrm{pu}] = f/f_n$. Wide view (a) and zoomed (b).

components. The discrete implementation of the SOGI-QSG is performed according to Algorithms 1 - 2 by means of a third-order integrator, which was shown in [16] to deliver the best results compared to other discretization techniques.

Algorithm 1 SOGI-QSG Algorithm

Input: $[x(n)]$
$\{y_\alpha(n)\} = \texttt{TO-Int}[(k_s(x(n) - y_\alpha(n-1)) - y_\beta(n-1))\omega_c]$
$\{y_\beta(n)\} = \texttt{TO-Int}[y_\alpha(n-1)]\omega_c$
Output: $\{y_\alpha(n), y_\beta(n)\}$

Algorithm 2 TO-Int Algorithm

Input: $[x(n)]$
$\zeta(n) = x(n)/(12 f_s) + \zeta(n-1)$
$\{y(n)\} = 23\zeta(n-1) - 16\zeta(n-2) + 5\zeta(n-3)$
Output: $\{y(n)\}$

III. The SOGI-IpDFT

A. Signal Model

As in [7], [12] the SOGI-IpDFT considers within the analysis window ($n \in [0, N-1]$) a static signal model composed of a fundamental tone and a potential interference tone, respectively, characterized by the parameter sets $\{A_0, f_0, \varphi_0\}$ and $\{A_i, f_i, \varphi_i\}$ denoting their amplitude, frequency, and initial phase:

$$x(n) = \underbrace{A_0 \cos(\omega_0 n T_s + \varphi_0)}_{\text{Fundamental Tone}} + \underbrace{A_i \cos(\omega_i n T_s + \varphi_i)}_{\text{Interference Tone}} \tag{9}$$

where $\omega_0 = 2\pi f_0$ and $\omega_i = 2\pi f_i$ denote the angular frequencies of the fundamental and interference tones. Given a set of N samples $x(n)$ (9), the algorithm provides estimates of the fundamental tone's parameters $\{\hat{A}_0, \hat{f}_0, \hat{\varphi}_0\}$. If detected, the effects of the interference tone are iteratively approximated and compensated, and estimates of its parameters can also be obtained $\{\hat{A}_i, \hat{f}_i, \hat{\varphi}_i\}$.

B. Proposed Method

The structure of the SOGI-IpDFT algorithm is summarized by the pseudocode in Algorithm 4, where the functions `SOGI-QSG`, `SOGI-CG`$_{\alpha\beta}$, `SOGI-CG`$_{+-}$, `e-IpDFT`, `DFT`, `IpDFT` and `wf` refer, respectively, to Algorithm 1, (7a)-(7b) evaluated at $j2\pi f_\gamma$, Algorithm 3, Algorithm 1 in [7], [12], the DFT, (2)-(3) and (4).

First, the in-quadrature signal components $(y_\alpha(n), y_\beta(n))$ are obtained by filtering the measured signal samples $(x(n))$ through Algorithm 1 (line 1), followed by the respective calculations of their DFT spectrums $(Y_\alpha(k), Y_\beta(k))$ and windowing (Hanning) in the frequency domain $(Y_{\alpha_H}(k), Y_{\beta_H}(k))$ (lines 2-4). An IpDFT is then applied to obtain a first estimate of the fundamental frequency of the signal $(\hat{f}_0)$ (line 5), which is used to calculate the fundamental complex α-β gains $(\sigma_{\alpha_0}, \sigma_{\beta_0})$ by means of (7a)-(7b) (line 8). Their magnitudes allow to correct the gains introduced by the SOGI-QSG filter at off-nominal frequencies (Fig. 2) and ensure equimagnitude between the in-quadrature components. Additionally, the windowed spectrum $(X_H(k))$ of the original measured signal samples is also determined (lines 6-7) as it is used to identify potential OOBIs. Subsequently, an interference compensation loop is initiated (line 10) after the initialization of two auxiliary variables (line 9). These are the initial estimate of the filtered spectrum of a potential interference tone $\hat{Y}_i^0(k)$ and the interference trigger flag τ_i.

Within the loop, an IpDFT is used first to estimate the parameters of the fundamental tone $(\hat{f}_0^q, \hat{A}_0^q, \hat{\varphi}_0^q)$ (lines 11-12). These are obtained by considering the magnitude-corrected bins of the windowed α-β spectrums $(Y_{\alpha_H}(k)/|\sigma_{\alpha_0}^{q-1}|, Y_{\beta_H}(k)/|\sigma_{\beta_0}^{q-1}|)$, and removing the estimated contribution of the filtered interference tone $(\hat{Y}_i^{q-1}(k))$. Then both $\sigma_{\alpha_0}^q$ and $\sigma_{\beta_0}^q$ are revised given the updated frequency $(\hat{f}_0^q)$ (line 13). During the first iteration ($q = 1$) the potential presence of an interference tone is analyzed (lines 14-21). The same procedure used in [7], [12] is adopted, which consists of determining the ratio between the total energy contained in the residual spectrum and that in the original spectrum and then comparing it to a threshold level defined heuristically (λ). To estimate $\hat{X}_i(k)$, the contribution of the fundamental tone is approximated given $\hat{f}_0^q$, $\hat{A}_0^q$ and $\hat{\varphi}_{0_x}^q$ and then subtracted from $X_H(k)$ (lines 16-17). The corrected phase of the signal $\hat{\varphi}_{0_x}^q$ is calculated by removing the phase shift introduced by the filter $\angle\sigma_{\alpha_0}$ (line 15).

If an interference tone is detected, an e-IpDFT is used to estimate its parameters (line 26) based on its β-component spectrum $(\hat{Y}_{i_\beta}^q(k))$. This spectrum is approximated by removing the contribution from the fundamental tone given $\hat{f}_0^q$, $\hat{A}_{0_\beta}^q$ and $\hat{\varphi}_{0_\beta}^q$ from $Y_{\beta_H}(k)$ (lines 23-25), where $\hat{A}_{0_\beta}^q$ and $\hat{\varphi}_{0_\beta}^q$ are the beta parameters of the fundamental tone calculated

Algorithm 3 SOGI-CG$_{+-}$ Algorithm

Input: $[\sigma_{\alpha_i}, \sigma_{\beta_i}, \sigma_{\alpha_0}, \sigma_{\beta_0}]$

$\sigma_{\alpha_+} = \sigma_{\alpha_i}/|\sigma_{\alpha_0}|; \sigma_{\beta_+} = \sigma_{\beta_i}/|\sigma_{\beta_0}|$

$\sigma_{\alpha_-} = \sigma_{\alpha_+}^*; \sigma_{\beta_-} = \sigma_{\beta_+}^*$

$\sigma_+ = \sigma_{\alpha_+} + j\sigma_{\beta_+}; \sigma_- = \sigma_{\alpha_-} + j\sigma_{\beta_-}$

Output: $\{\sigma_+, \sigma_-\}$

Algorithm 4 SOGI-IpDFT Algorithm

Input: $[x(n)]$

1: $\{y_\alpha(n), y_\beta(n)\} = \texttt{SOGI-QSG}[x(n)]$

2: $Y_\alpha(k) = \texttt{DFT}[y_\alpha(n)]; Y_\beta(k) = \texttt{DFT}[y_\beta(n)];$

3: $Y_{\alpha_H}(k) = 0.5Y_\alpha(k) - 0.25(Y_\alpha(k-1) + Y_\alpha(k+1))$

4: $Y_{\beta_H}(k) = 0.5Y_\beta(k) - 0.25(Y_\beta(k-1) + Y_\beta(k+1))$

5: $\{\hat{f}_0\} = \texttt{IpDFT}[Y_{\alpha_H}(k) + jY_{\beta_H}(k)]$

6: $X(k) = \texttt{DFT}[x(n)]$

7: $X_H(k) = 0.5X(k) - 0.25(X(k-1) + X(k+1))$

8: $\{\sigma_{\alpha_0}^0, \sigma_{\beta_0}^0\} = \texttt{SOGI-CG}_{\alpha\beta}[\hat{f}_0]$

9: **Initialization:** $\hat{Y}_i^0(k) = 0; \tau_i = 0$

10: **for** $q = 1$ **to** Q **do**

11: $\{\hat{f}_0^q, \hat{A}_0^q, \hat{\varphi}_0^q\} = \texttt{IpDFT}\left[\frac{Y_{\alpha_H}(k)}{|\sigma_{\alpha_0}^{q-1}|} + j\frac{Y_{\beta_H}(k)}{|\sigma_{\beta_0}^{q-1}|} - \hat{Y}_i^{q-1}(k)\right]$

12: $\hat{A}_0^q = \hat{A}_0^q/2$

13: $\{\sigma_{\alpha_0}^q, \sigma_{\beta_0}^q\} = \texttt{SOGI-CG}_{\alpha\beta}[\hat{f}_0^q]$

14: **if** $q = 1$ **then**

15: $\hat{\varphi}_{0_x} = \hat{\varphi}_0 - \angle\sigma_{\alpha_0}$

16: $\hat{X}_0(k) = \texttt{wf}[\hat{f}_0, \hat{A}_0, \hat{\varphi}_{0_x}] + \texttt{wf}[-\hat{f}_0, \hat{A}_0, -\hat{\varphi}_{0_x}]$

17: $\hat{X}_i(k) = X_H(k) - \hat{X}_0(k)$

18: **if** $\sum|\hat{X}_i(k)|^2 > \lambda\sum|X_H(k)|^2$ **then**

19: $\tau_i = 1$

20: **end if**

21: **end if**

22: **if** $\tau_i = 1$ **then**

23: $\hat{A}_{0_\beta}^q = \hat{A}_0^q|\sigma_{\beta_0}^q|; \hat{\varphi}_{0_\beta}^q = \hat{\varphi}_0^q - \pi/2$

24: $\hat{Y}_{0_\beta}^q(k) = \texttt{wf}[\hat{f}_0^q, \hat{A}_{0_\beta}^q, \hat{\varphi}_{0_\beta}^q] + \texttt{wf}[-\hat{f}_0^q, \hat{A}_{0_\beta}^q, -\hat{\varphi}_{0_\beta}^q]$

25: $\hat{Y}_{i_\beta}^q(k) = Y_{\beta_H}(k) - \hat{Y}_{0_\beta}^q(k)$

26: $\{\hat{f}_i^q, \hat{A}_{i_\beta}^q, \hat{\varphi}_{i_\beta}^q\} = \texttt{e-IpDFT}[\hat{Y}_{i_\beta}^q(k)]$

27: $\{\sigma_{\alpha_i}^q, \sigma_{\beta_i}^q\} = \texttt{SOGI-CG}_{\alpha\beta}[\hat{f}_i^q]$

28: $\hat{A}_i^q = \hat{A}_{i_\beta}^q/|\sigma_{\beta_i}^q|; \hat{\varphi}_i^q = \hat{\varphi}_{i_\beta}^q - \angle\sigma_{\beta_i}^q$

29: $\{\sigma_+^q, \sigma_-^q\} = \texttt{SOGI-CG}_{+-}[\sigma_{\alpha_i}^q, \sigma_{\beta_i}^q, \sigma_{\alpha_0}^q, \sigma_{\beta_0}^q]$

30: $\hat{A}_{i+}^q = \hat{A}_i^q|\sigma_+^q|; \hat{A}_{i-}^q = \hat{A}_i^q|\sigma_-^q|$

31: $\hat{\varphi}_{i+}^q = \hat{\varphi}_i^q + \angle\sigma_+^q; \hat{\varphi}_{i-}^q = -\hat{\varphi}_i^q + \angle\sigma_-^q$

32: $\hat{Y}_i^q(k) = \texttt{wf}[\hat{f}_i^q, \hat{A}_{i+}^q, \hat{\varphi}_{i+}^q] + \texttt{wf}[-\hat{f}_i^q, \hat{A}_{i-}^q, \hat{\varphi}_{i-}^q]$

33: **else**

34: **break**

35: **end if**

36: **end for**

37: $\hat{\varphi}_0^q = \hat{\varphi}_0^q - \angle\sigma_{\alpha_0}^q$

Output: $\{\hat{f}_0, \hat{A}_0, \hat{\varphi}_0\}$

according to the filter response. The actual magnitude and phase ($\hat{A}_i^q$, $\hat{\varphi}_i^q$) of the interference tone are then obtained by removing the effects of the SOGI-QSG filter at the frequency of the tone $\hat{f}_i^q$ based on the calculated interference complex α-β gains ($\sigma_{\alpha_i}^q, \sigma_{\beta_i}^q$) (lines 27-28). Algorithm 3 is then used to aggregate the effects of the positive and negative images of the interfering tone from both in-quadrature components while also considering the magnitude correction applied to the windowed α-β spectra and used for the fundamental estimation (line 29). The obtained interference complex positive and negative gains ($\sigma_{+_i}^q, \sigma_{-_i}^q$) are used to estimate the filtered spectrum of the interference tone $\hat{Y}_i^q(k)$ (lines 30-32) and enhance the fundamental estimate in the next iteration. The process is looped Q times. The final results, the initial estimate, if no interferences are found, or the latest once the maximum number of iterations is reached, are then phase corrected to account for the phase shift of the filter (line 37). Since the frequency time derivative is not part of the signal model, the Rate-Of-Change-Of-Frequency (ROCOF) at the reporting time m is calculated based on fundamental frequency estimates at two successive reporting times (m and $m-1$) with a first-order backward approximation of a first-order derivative:

$$\dot{\hat{f}}_0(m) = \left(\hat{f}_0(m) - \hat{f}_0(m-1)\right) F_r \tag{10}$$

where F_r denotes the reporting rate.

C. Parametrization and Computational Cost

The computational complexity of the SOGI-IpDFT is now analyzed to compare its performance with other state-of-the-art techniques such as the i-IpDFT [7], [12] and evaluate the viability of its potential implementation in an embedded device. The analysis is done in terms of the total number of arithmetic operations required by the SOGI-IpDFT (both in case an interference tone is detected or not) versus those used by its constituent functions, e.g., `IpDFT`.

A distinction between simple operations ($+\ -\ \times$), complex operations ($\div\ \sin\ |...|\ \angle$), and function calls (such as calls to predefined subroutines or algorithms, e.g. `IpDFT`) is drawn as in [5], [7]. All are formulated in terms of the total number of calculated DFT bins K, and the maximum number of executions of the iterative process Q. The results show for a case of no interference a total requirement of 1274 simple and 168 complex operations, while $1179 + 1501$Q simple and $155 + 446$Q complex operations are needed considering the OOBI iterative compensation for 8 DFT bins.

To facilitate the analysis, the algorithm is parameterized according to Table I. For method-specific parameters, '-' is indicated for the non-applicable algorithm. To make a fair comparison, the same values are selected for both the SOGI-IpDFT and the i-IpDFT for shared parameters based on the values presented in [12]. The only exception is for the maximum number of iterations Q for the OOBI correction.

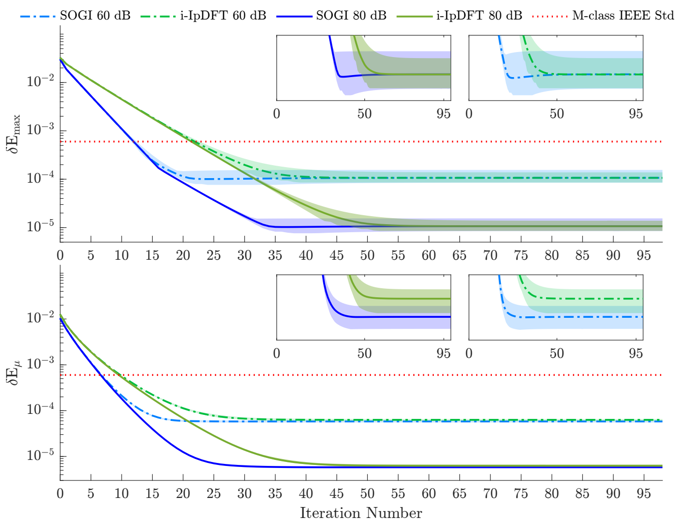

Fig. 3. Performance comparison between SOGI-IpDFT and i-IpDFT for noise levels with signal-to-noise ratios (SNR) equal to 60 and 80 dB for 25 different runs. $\delta E_{\max}$ (top) and δE_{μ} (bottom) as a function of the maximum iteration number Q. The shaded areas are given by the maximum-minimum value pairs of $\delta E_{\max}$ and δE_{μ} while the solid (80 dB) and dotted-dashed (60 dB) lines represent their mean values across all runs. Zoomed plots of the shaded areas are provided to show the variability caused by noise.

The tuning of this parameter is done according to $\delta E_{\max}$ (11a) and δE_{μ} (11b). These are defined as:

$$\delta E_{\max} = \max_{f_i} \left(\max_{f_0} \left(\delta E_{f_0 f_i} \right) \right) \tag{11a}$$

$$\delta E_{\mu} = \frac{1}{\# F_i} \sum_{f_i} \left(\max_{f_0} \left(\delta E_{f_0 f_i} \right) \right) \tag{11b}$$

where $\delta E_{f_0 f_i}$ is the error in estimating the correction term δ (2) given a signal characterized by a fundamental frequency f_0 and a 10% interference signal f_i, F_i is the set of considered OOBI signal frequencies and $\#$ denotes cardinality. $\delta E_{\max}$ represents the maximum error obtained in estimating the correction term δ (2) for all interferences and fundamental frequency values, while δE_{μ} is the mean error across the OOBI range considering the largest error that each interference produces for each fundamental frequency. The values considered for f_0 and the set F_i of interference frequencies are selected in accordance with [8] for a F_r of 50 fps. A performance comparison between the SOGI-IpDFT and the i-IpDFT is shown in Fig. 3 as a function of Q. The figure reports $\delta E_{\max}$ and δE_{μ} for noise levels with SNR equal to 60 and 80 dB for 25 different runs. The shaded areas are given by the maximum-minimum value pairs of $\delta E_{\max}$ and δE_{μ} while the solid (80 dB) and dotted-dashed (60 dB) lines represent their mean values across all runs. The results reveal similar variability due to noise for both methods in terms of δE_{μ} while a higher impact is observed in terms of $\delta E_{\max}$ for the SOGI-IpDFT. However, in terms of the mean values obtained, it is seen, regardless of the noise level considered, that the SOGI-IpDFT requires fewer iterations to achieve the same performance as the i-IpDFT in terms of $\delta E_{\max}$. Also, in terms of δE_{μ} the i-IpDFT cannot match the performance of

TABLE I
SOGI-IpDFT and i-IpDFT parameters

Parameter	Variable	Value	
		SOGI-IpDFT	i-IpDFT
Nominal System Frequency	f_n	50 Hz	50 Hz
Window Type	-	Hann	Hann
Window Length	T	60 ms ($\frac{3}{f_n}$)	60 ms ($\frac{3}{f_n}$)
Sampling Rate	F_s	50 kHz	50 kHz
PMU Reporting Rate	F_r	50 fps	50 fps
DFT bins	K	8	8
Self-Inter. comp. (fund)	P_0	-	1
Self-Inter. comp. (inter)	P_i	2	2
Max Number of Iterations	Q	35	71
IpDFT Interpolation Points	-	3	3
OOBI Detection Threshold	λ	$3.3 \cdot 10^{-3}$	$3.3 \cdot 10^{-3}$
Settling Time	t_s	20 ms	-
Filter Centre Frequency	ω_c	$2\pi f_n$	-
SOGI-QSG Gain	k_s	$9.2/(t_s\omega_c)$	-

TABLE II
SOGI-IpDFT Computational Complexity

		Parameter	Value
		q	$\leq$ Q
		K	8
	$+\ -\ \times$	$\div$ sin $\lvert ... \rvert$ $\angle$	$g(h)$
(h_1) `IpDFT` (3p)	15	8	-
(h_2) `wf`	24K+15	7K+10	-
(h_3) `SOGI-QSG`	5	0	$2h_4$
(h_4) `TO-Int`	7	0	-
(h_5) `SOGI-CG`$_{\alpha\beta}$	15	1	-
(h_6) `SOGI-CG`$_{+-}$	10	4	-
(h_7) `e-IpDFT` (P_i= 2)	4K+4	0	$3h_1$+$2h_2$
(h_8) `mSDFT`	17K+18	0	-
Alg. IV	$+\ -\ \times$	$\div$ sin $\lvert ... \rvert$ $\angle$	$g(h)$
`SOGI-IpDFT` (no int.)	40K+14	2K+10	$h_{1,3}$+$2h_{2,5}$ +$3h_8$
`SOGI-IpDFT` (OOBI)	32K+13 +14KQ +11Q	2K+6 +12Q	Q$h_{1,6,7}$+ (1+2Q)(h_5+ $2h_2$)+h_3+$3h_8$

the SOGI-IpDFT for the entire range of simulated Q values. A $Q = 71$ is selected for the i-IpDFT as it corresponds to the intersection value between the two methods for $\delta E_{\max}$ and 80 dB. To ensure an equivalent level of performance, a $Q = 35$ should be selected for the SOGI-IpDFT. However, a value of $Q = 38$ is recommended since it results in the minimum value of $\delta E_{\max}$ for the method with 80 dB noise. In general, approximately a 55.2% reduction in total computational cost is achieved with the SOGI-IpDFT compared to the i-IpDFT if a $Q = 35$ is selected for the first, while a 51.5% is achieved instead if $Q = 38$ is used. However, this comes at the expense of tripling the required signal buffer size as shown in Fig. 8 for a mSDFT [17] based implementation. In any case, this only represents a total buffer size of 72 kB based on the values of T and F_s in Table I and the MATLAB double numeric data type.

IV. Performance Assessment

In this section, the performance of the SOGI-IpDFT algorithm is evaluated against the static and dynamic accuracy limits set by the standard for the P and M classes [8] and compared with that of the i-IpDFT proposed in [7], [12]. Validation is carried out in a MATLAB simulated environment in terms of total vector error (TVE), frequency error (FE), and ROCOF error (RFE), as well as response times (R_t), delay times (D_t) and maximum overshoot values for the step tests. All simulations are carried out according to the parameters given in Table I considering test signals affected by two levels of additive white Gaussian noise. Equivalent parameters are adopted for both methods to ensure a fair comparison. As in [7], noise levels with SNRs equal to 60 and 80 dB have been selected to account for the uncertainty of the measurement and simulate more realistic conditions. The results of all tests for both the SOGI-IpDFT and the i-IpDFT are graphed against the accuracy limits defined in [8] in Figs. 4 - 7. Plots for static and dynamic tests are shown for both 60 dB and 80 dB noise levels, while step tests are only shown for 80 dB for better clarity. Furthermore, the maximum values of both algorithms are summarized in Tables III, IV, and V.

A. Static Tests

The results of all the static tests defined in [8] are presented in Figs. (4 - 5) and Table III. The signal frequency range test (Fig. 4(a)) shows how the frequency of the fundamental tone does not affect the accuracy of neither method. The SOGI-IpDFT also achieves slightly higher accuracy in all metrics compared to the i-IpDFT. Maximum errors of 0.018% (60 dB) and 0.002% (80 dB) for the TVE, 1.01 mHz (60 dB) and 0.10 mHz (80 dB) for the FE and 0.084 Hz/s (60 dB) and 0.008 Hz/s (80 dB) for the ROCOF are obtained and reported in Table III for the SOGI-IpDFT, which comply with their respective most restrictive limits of 1%, 5mHz and 0.1 Hz/s. As observed in [7] for the i-IpDFT, both algorithms present spurious RFE values that can marginally exceed the most stringent limit of class M under the higher SNR of 60 dB solely due to noise. Compliance is also proven for the harmonic distortion test, where Table III shows the maximum errors obtained for THDs of 1% and 10%. For the most challenging noise level (60 dB), the maximum reported TVE values of 0.019% are well below the 1% limit. Similarly, the maximum values of FE and RFE were 1.01 mHz, 1.07 mHz for the frequency, and 0.084 Hz/s and 0.089 Hz/s for the ROCOF, which are within the more demanding P-class requirements. The results of the harmonic distortion test for a THD of 10% are shown in Fig. 4(b) where both methods exhibit almost equivalent error levels.

For the OOBI test, the maximum values of TVE, FE and RFE obtained for each interference tone among the three simulated fundamental frequency values of 47.5, 50 and 52.5 Hz are shown in Fig. 5. A total interharmonic distortion of 10% has been considered, as required by [8]. The maximum values obtained segregated per fundamental frequency are summarized in Table III and are shown to be well within the performance requirements of class M. All static tests reveal how the precision is determined by the total noise level present in the signal and not, respectively, by the fundamental tone frequency (signal frequency range test), the order of the interfering harmonic tone (harmonic distortion test), or that of the subharmonic or interharmonic tone (OOBI test).

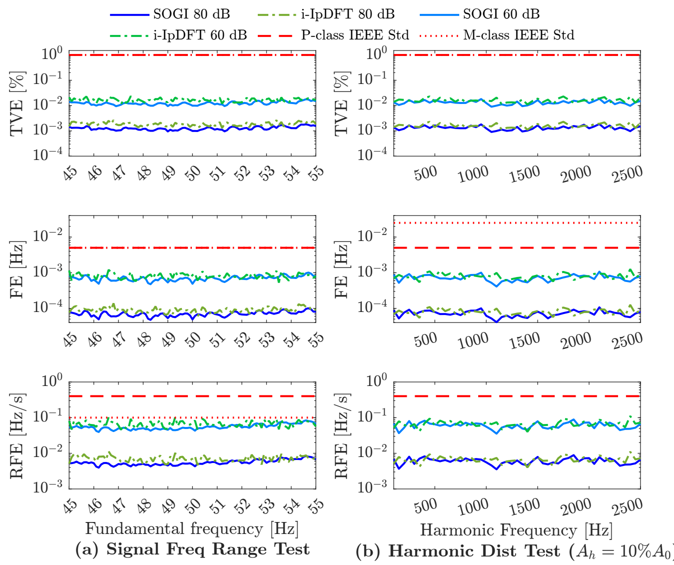

Fig. 4. Static tests: (a) Signal frequency range test and (b) Harmonic distortion test ($A_h = 10\% A_0$) [8].

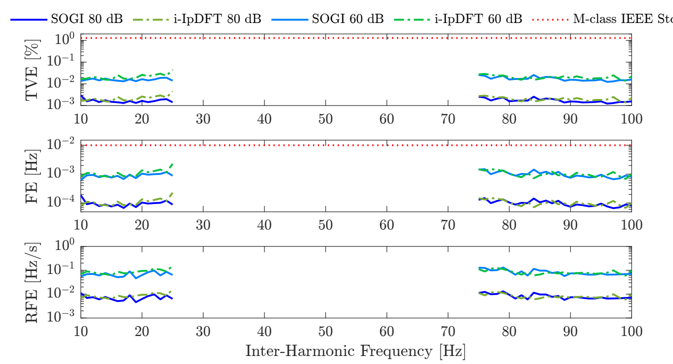

Fig. 5. OOBI test ($A_{ih} = 10\% A_0$) [8].

B. Dynamic Tests

The results of all dynamic tests defined in [8] are presented in Fig. 6 and Table IV. As shown in Fig. 6 the maximum errors obtained by both algorithms comply with the most demanding requirements set in [8]. These correspond, respectively, to class P for the measurement bandwidth test and class M for the frequency ramp test. The maximum overall error values are summarized in Table IV. For the measurement bandwidth tests, both Fig. 6 (a), in the case of amplitude modulation, and Fig. 6 (b), for phase modulation, depict the maximum errors obtained with each algorithm for modulating frequencies between 0.1 and 5Hz, while the worst-case results of the frequency ramp test are shown in Fig. 6 (c) for different positive and negative ramp rates.

TABLE III
Maximum TVE, FE and RFE in Static Tests and Maximum Limit Allowed by [8]

	TVE[%]						FE[mHz]						RFE[Hz/s]					
	IEEE Std		Hann $(3/f_n)$				IEEE Std		Hann $(3/f_n)$				IEEE Std		Hann $(3/f_n)$			
	P	M	SOGI		i-IpDFT		P	M	SOGI		i-IpDFT		P	M	SOGI		i-IpDFT	
SNR [dB]			60	80	60	80			60	80	60	80			60	80	60	80
Sign Freq	1	1	0.018	0.002	0.024	0.003	5	5	1.01	0.10	1.21	0.14	0.4	0.1	0.084	0.008	0.104	0.011
Harm Dist 1%	1	1	0.019	0.002	0.022	0.002	5	25	1.01	0.10	1.10	0.11	0.4	-	0.084	0.008	0.089	0.009
Harm Dist 10%	1	1	0.019	0.002	0.023	0.002	5	25	1.07	0.11	1.26	0.13	0.4	-	0.089	0.009	0.111	0.011
OOBI 47.5Hz	-	1.3	0.019	0.002	0.045	0.005	-	10	1.18	0.13	2.28	0.23	-	-	0.098	0.010	0.159	0.016
OOBI 50Hz	-	1.3	0.018	0.003	0.028	0.003	-	10	1.20	0.19	1.24	0.12	-	-	0.087	0.011	0.118	0.012
OOBI 52.5Hz	-	1.3	0.026	0.003	0.029	0.003	-	10	1.49	0.15	1.50	0.15	-	-	0.131	0.013	0.123	0.012

TABLE IV
Maximum TVE, FE and RFE in Dynamic Tests and Maximum Limit Allowed by [8]

	TVE[%]						FE[mHz]						RFE[Hz/s]					
	IEEE Std		Hann $(3/f_n)$				IEEE Std		Hann $(3/f_n)$				IEEE Std		Hann $(3/f_n)$			
	P	M	SOGI		i-IpDFT		P	M	SOGI		i-IpDFT		P	M	SOGI		i-IpDFT	
SNR [dB]			60	80	60	80			60	80	60	80			60	80	60	80
Ampl Mod	3	3	0.694	0.692	0.607	0.604	60	300	26.73	26.49	1.20	0.45	2.3	14	0.797	0.762	0.092	0.016
Ph Mod	3	3	0.605	0.602	0.551	0.547	60	300	19.89	19.69	17.94	17.40	2.3	14	0.900	0.867	0.862	0.802
Freq Ramp	1	1	0.049	0.042	0.043	0.038	10	10	1.10	0.11	1.15	0.15	0.4	0.2	0.099	0.010	0.109	0.011

Both the SOGI-IpDFT and the i-IpDFT show no significant differences in performance in terms of frequency ramps or phase modulations. The frequency ramp test results in FE and RFE values equivalent to those of the signal frequency test regardless of the ramp rate and increasing TVEs with higher ramp rate magnitudes. At the same time, under phase modulations, increasing modulating frequencies result in higher TVEs, FEs, and RFEs, which eventually substitute noise as the main source of error. The same is observed in terms of ramp rates for the TVE in the frequency ramp test.

Finally, in the case of amplitude modulations, more accurate results are obtained using the i-IpDFT. This is especially noticeable in terms of FE and RFE, where the values achieved by the i-IpDFT are less affected by (80 dB) or independent of (60 dB) the modulating frequency. These results reveal that the e-IpDFT [6] routine on which the i-IpDFT is based has a more robust behavior in this case compared to the SOGI-QSG filter.

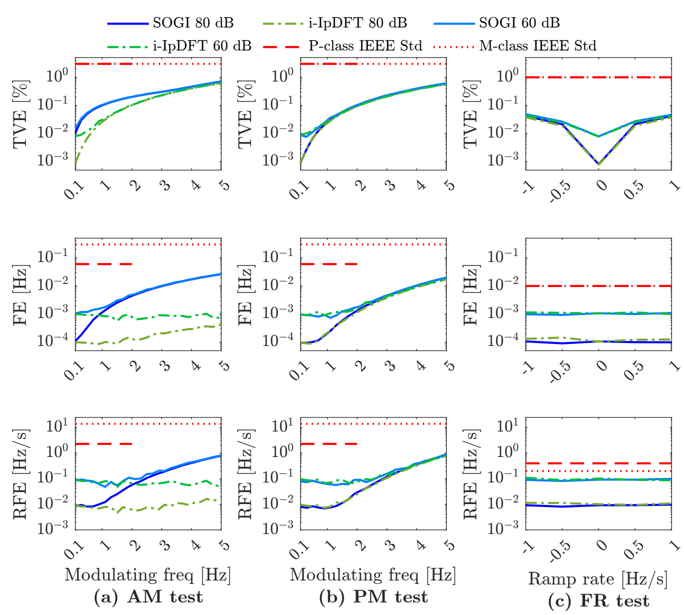

Fig. 6. Dynamic tests: (a) Amplitude modulation test (depth 10%); (b) Phase modulation test (depth $\pi/18$ rad); and (c) Frequency ramp test [8].

C. Step Tests

The results of both step tests defined in [8] are presented in Fig. 7, and their response times, delay times, and maximum overshoot values are presented in Table V. All results correspond to the positive step cases (similar results are obtained in the case of negative steps) and are only graphed for 80 dB noise for better clarity.

TVE, FE, and RFE are represented in Fig. 7 as a function of their respective response times, that is, the origin of each time axis corresponds to the moment when the accuracy limit is first exceeded. Similarly, the estimated phase and amplitude are shown as functions of their respective delay times, i.e. the origin of the time axis is the instant at which each step occurs. The results show how both algorithms meet all requirements, and although slightly higher response times are obtained for the SOGI-IpDFT in terms of FE and RFE, all estimates are within the limits. Similarly, higher levels of overshoot are obtained for SOGI-IpDFT compared to those obtained for the

TABLE V
MAXIMUM RESPONSE, DELAY TIMES, AND OVERSHOOTS IN STEP TESTS AND LIMITS ALLOWED BY [8]

	TVE Response Time [ms]						FE Response Time [ms]						RFE Response Time [ms][a]					
	IEEE Std		Hann $(3/f_n)$				IEEE Std		Hann $(3/f_n)$				IEEE Std		Hann $(3/f_n)$			
	P	M	SOGI		i-IpDFT		P	M	SOGI		i-IpDFT		P	M	SOGI		i-IpDFT	
SNR [dB]			60	80	60	80			60	80	60	80			60	80	60	80
Ampl Step	40	140	30	30	28	28	90	280	56	56	46	46	120	280	110	82	104	68
Ph Step	40	140	36	36	34	34	90	280	58	58	48	48	120	280	106	88	104	72

	Delay Time [ms]						Max Overshoot [%]					
	IEEE Std		Hann $(3/f_n)$				IEEE Std		Hann $(3/f_n)$			
	P	M	SOGI		i-IpDFT		P	M	SOGI		i-IpDFT	
SNR [dB]			60	80	60	80			60	80	60	80
Ampl Step	5	5	0	0	2	2	5	10	0.170	0.139	0.077	0.008
Ph Step	5	5	0	0	2	2	5	10	0.281	0.260	0.047	0.005

[a] The RFE response times have been calculated considering all crossings with the M class accuracy band limit of 0.1 Hz/s within a 140 ms window centered around the step. This is done to exclude spurious RFE values that marginally exceed the said limit under the higher SNR of 60 dB solely due to noise.

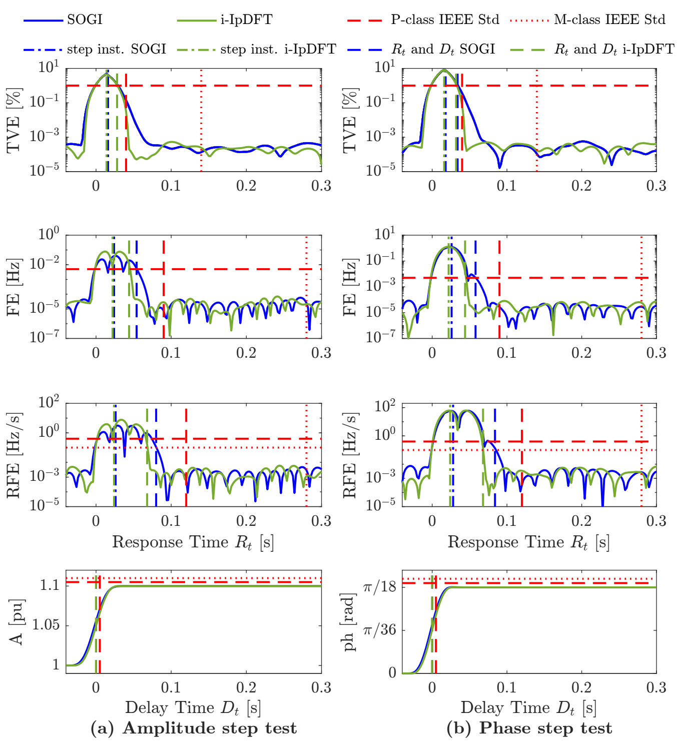

Fig. 7. Step tests: (a) Amplitude step test (+10%) and (b) Phase step test (+π/18) [8].

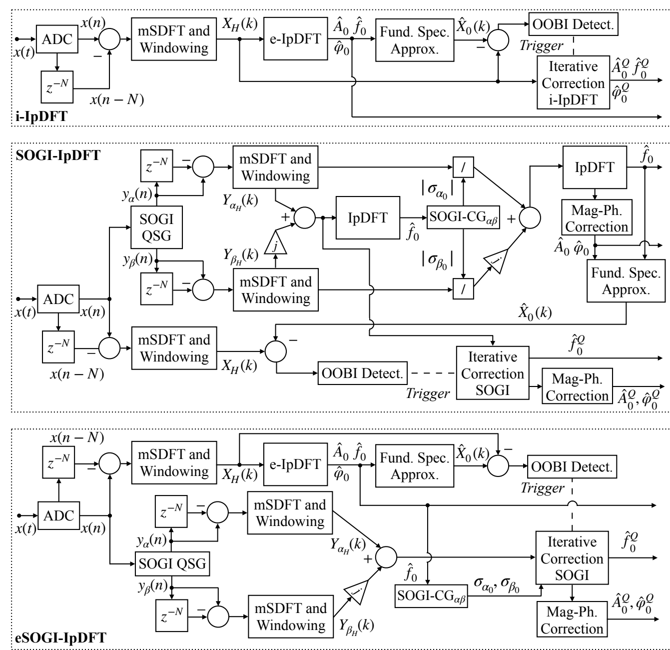

Fig. 8. Diagrams of the i-IpDFT, the SOGI-IpDFT and the eSOGI-IpDFT. The mSDFT [17] is used to calculate the required DFT bins.

i-IpDFT. However, in both cases, these are well below the limit set in the standard.

V. DISCUSSION

Overall, given the results of the comparative analysis between the SOGI-IpDFT and the i-IpDFT, it can be concluded that the combination of the two SE methods would offer significant advantages. An algorithm relying on the SOGI-QSG filter for the iterative process whenever an OOBI is detected, and the e-IpDFT routine otherwise, would guarantee a performance equivalent to that of the i-IpDFT with a reduced computational cost equal to that of the SOGI-IpDFT. Fig. 8 summarizes the structure of the i-IpDFT, the SOGI-IpDFT and the merged algorithm, named eSOGI-IpDFT which does not require any additional parametric adjustment. Another feature offered by the SOGI-IpDFT, and exploitable in the eSOGI-IpDFT, is the availability of a complex signal at the SOGI-QSG filter output. Potentially both the amplitude and phase of this signal could be used to develop and implement detection and correction techniques for the amplitude and phase steps as shown in [18].

VI. CONCLUSIONS

In this article, a SE technique has been presented to combine the application of a SOGI-QSG filter with the IpDFT. The resulting filtered complex signal has a spectrum characterized by an attenuated self-interference of the fundamental tone, which allows a reduction in the total computational complexity of 55.2% compared to the i-IpDFT when the OOBI routine is activated for an equivalent level of performance.

A complete assessment of the proposed method has shown that it satisfies all the accuracy requirements defined in the IEC/IEEE Std. 60255-118 for both the P and M classes. The method achieves a performance equivalent to that of the i-IpDFT in all cases, except for the amplitude modulation test, where the SOGI-IpDFT is shown to deliver less accurate estimates, and the step tests where slightly higher response times and overshoot values are obtained for the SOGI-IpDFT. Overall, a combination of the SOGI-QSG filter when an OOBI is detected and the e-IpDFT routine otherwise would guarantee a performance equivalent to that of the i-IpDFT with a reduced computational cost equal to that of the SOGI-IpDFT.

References

[1] I. Kamwa, S. R. Samantaray, and G. Joos, "Wide frequency range adaptive phasor and frequency pmu algorithms," *IEEE Trans. Smart Grid*, vol. 5, no. 2, pp. 569–579, Mar. 2014.

[2] D. Belega, D. Petri, and D. Dallet, "Frequency estimation of a sinusoidal signal via a three-point interpolated dft method with high image component interference rejection capability," *Digit. Signal Process.*, vol. 24, pp. 162–169, Jan. 2014.

[3] V. K. Jain, W. L. Collins, and D. C. Davis, "High-accuracy analog measurements via interpolated fft," *IEEE Trans. Instrum. Meas.*, vol. 28, no. 2, pp. 113–122, Jun. 1979.

[4] F. J. Harris, "On the use of windows for harmonic analysis with the discrete fourier transform," *Proc. IEEE*, vol. 66, no. 1, pp. 51–83, Jan. 1978.

[5] G. Frigo, A. Derviškadić, and M. Paolone, "Reduced leakage synchrophasor estimation: Hilbert transform plus interpolated dft," *IEEE Trans. Instrum. Meas.*, vol. 68, no. 10, pp. 3468–3483, Oct. 2019.

[6] P. Romano and M. Paolone, "Enhanced interpolated-dft for synchrophasor estimation in fpgas: Theory, implementation, and validation of a pmu prototype," *IEEE Trans. Instrum. Meas.*, vol. 63, no. 12, pp. 2824–2836, Dec. 2014.

[7] A. Derviškadić, P. Romano, and M. Paolone, "Iterative-interpolated dft for synchrophasor estimation: A single algorithm for p-and m-class compliant pmus," *IEEE Trans. Instrum. Meas.*, vol. 67, no. 3, pp. 547–558, Mar. 2018.

[8] "IEEE/IEC International Standard - Measuring relays and protection equipment - Part 118-1: Synchrophasor for power systems - Measurements," *IEC/IEEE 60255-118-1:2018*, pp. 1–78, 2018.

[9] D. Agrež, "Weighted multipoint interpolated dft to improve amplitude estimation of multifrequency signal," *IEEE Trans. Instrum. Meas.*, vol. 51, no. 2, pp. 287–292, Apr. 2002.

[10] D. Belega and D. Petri, "Sine-wave parameter estimation by interpolated dft method based on new cosine windows with high interference rejection capability," *Dig. Signal Process.*, vol. 33, pp. 60–70, Oct. 2014.

[11] C. García-Veloso, M. Paolone, and J. M. Maza-Ortega, "Computationally-efficient synchrophasor estimation: Delayed in-quadrature interpolated dft," 2023. arXiv: 2304.07634.

[12] A. Derviškadić and M. Paolone, "Design and experimental validation of an fpga-based pmu simultaneously compliant with p and m performance classes," *Electr. Power Syst. Res.*, vol. 189, Dec. 2020, Art. no. 106650.

[13] T. Grandke, "Interpolation algorithms for discrete fourier transforms of weighted signals," *IEEE Trans. Instrum. Meas.*, vol. 32, no. 2, pp. 350–355, Jun. 1983.

[14] S. Golestan, J. M. Guerrero, and J. C. Vasquez, "Single-phase plls: A review of recent advances," *IEEE Trans. Power Electron.*, vol. 32, no. 12, pp. 9013–9030, Dec. 2017.

[15] R. Teodorescu, M. Liserre, and P. Rodríguez, "Grid synchronization in single-phase power converters," in John Wiley & Sons, Ltd, 2011, ch. 4, pp. 43–91.

[16] M. Ciobotaru, R. Teodorescu, and F. Blaabjerg, "A new single-phase pll structure based on second order generalized integrator," in *Proc. IEEE 37th Power Electron. Specialists Conf.*, 2006, pp. 1–6.

[17] K. Duda, "Accurate, guaranteed stable, sliding discrete fourier transform [DSP tips & tricks]," *IEEE Signal Process. Mag.*, vol. 27, no. 6, pp. 124–127, Nov. 2010.

[18] A. Karpilow, M. Paolone, A. Derviškadić, and G. Frigo, "Step change detection for improved rocof evaluation of power system waveforms," in *Proc. Int. Conf. Smart Grid Synchronized Meas. Anal.*, 2022, pp. 1–7.